Long-Term Observations of the Dynamics of the Continental Planetary Boundary Layer

Chuixiang Yi,* Kenneth J. Davis,[+] and Bradford W. Berger[#]

Department of Soil, Water and Climate, University of Minnesota, St. Paul, Minnesota

Peter S. Bakwin

Climate Monitoring and Diagnostics Laboratory, National Oceanic and Atmospheric Administration, Boulder, Colorado

ABSTRACT

Time series of mixed layer depth, z_i, and stable boundary layer height from March through October of 1998 are derived from a 915-MHz boundary layer profiling radar and CO_2 mixing ratio measured from a 447-m tower in northern Wisconsin. Mixed layer depths from the profiler are in good agreement with radiosonde measurements. Maximum z_i occurs in May, coincident with the maximum daytime surface sensible heat flux. Incoming radiation is higher in June and July, but a greater proportion is converted to latent heat by photosynthesizing vegetation. An empirical relationship between z_i and the square root of the cumulative surface virtual potential temperature flux is obtained ($r^2 = 0.98$) allowing estimates of z_i from measurements of virtual potential temperature flux under certain conditions. In fair-weather conditions the residual mixed layer top was observed by the profiler on several nights each month. The synoptic mean vertical velocity (subsidence rate) is estimated from the temporal evolution of the residual mixed layer height during the night. The influence of subsidence on the evolution of the mixed, stable, and residual layers is discussed. The CO_2 jump across the inversion at night is also estimated from the tower measurements.

1. Introduction

The depth of the planetary boundary layer (PBL) and the intensity of the turbulence within it have a strong impact on the vertical and horizontal distribution of CO_2 in the atmosphere (Denning et al. 1995; Wofsy et al. 1988). During the daytime in summer the influence of photosynthetic uptake on the mixing ratio of CO_2 is diluted by deep convective turbulent mixing. The influence of respiration on the CO_2 mixing ratio at night is amplified near the surface by a shallow, stable boundary layer. The covariance between surface fluxes of CO_2 and the vigor of atmospheric mixing, which has been termed the ''rectifier effect'' (Denning et al. 1999; Law and Rayner 1999), has a strong seasonal character, with deeper convection during the daytime in summer when photosynthesis exceeds respiration (Denning et al. 1996). Observed distributions of CO_2 have been used to calculate spatial distributions of sources and sinks by inverse methods (e.g., Tans et al. 1990; Ciais et al. 1995; Francey et al. 1995; Fan et al. 1998). Since the rectifier effect influences the horizontal and vertical distributions of CO_2 in the atmosphere, it can lead to a serious bias in the calculated fluxes if not properly accounted for in inverse models (Denning et al. 1995). In order to study the diurnal and seasonal patterns of the rectifier effect, long-term, continuous observations of PBL dynamics and CO_2 mixing ratios over the continents are imperative.

Long-term, continuous observations of PBL structure were difficult or impossible until the recent development of robust boundary layer profiling radar and Radio-Acoustic Sounding System (RASS) (Ecklund et al. 1988). Most deployments of these systems to date have been too brief to capture seasonal information. For this study a radar profiler, RASS, and radiosonde system were deployed for the period from 15 March to 3 November 1998, near to a 447-m tall TV transmitter tower in northern Wisconsin. The tower was instrumented to measure continuously the turbulent flux profiles of latent and sensible heat, and flux and mixing ratio profiles of

* Permanent affiliation: Key Laboratory of Environmental Change and Natural Disaster, Ministry of Education, Beijing, China.

[+] Current affiliation: Department of Meteorology, The Pennsylvania State University, University Park, Pennsylvania.

[#] Current affiliation: Department of Mathematics and Statistics, University of Edinburgh, Edinburgh, Scotland.

Corresponding author address: Chuixiang Yi, Department of Meteorology, The Pennsylvania State University, 416 Walker Building, University Park, PA 16802.
E-mail: cxyi@essc.psu.edu

CO_2. Daytime convective PBL (mixed layer) depth measurements from the radar were verified against data from radiosondes.

Measurements of the vertical profile of CO_2 mixing ratio on the TV tower allowed us to study the evolution of the stable PBL at night. The stable layer is typically very shallow, usually less than 200 m, and therefore is not accessible to the profiler and RASS, which have a minimum altitude of 150 m above the ground with 60-m sampling interval.

Three to four days per month we were able to observe at night the height of the residual mixed layer from the previous day. These weather conditions were characterized by calm, fair-weather conditions, high surface pressure, and subsidence. From the rate of change of the residual-layer depth, we obtain an estimate of the subsidence rate, which was typically in the range 1–3 cm s^{-1}. These results provide a valuble and unique dataset to check subsidence estimates from weather prediction models. We also estimate the influence of subsidence on the structure of the mixed and stable layers.

2. Study site and measurements

The study site is located in Chequamegon National Forest in northern Wisconsin. The region is in a heavily forested zone of low relief. The tower is a 447-m tall television transmitter surrounded by a grassy clearing of about 180-m radius. The site, instrumentation, and flux calculation methodology have been described by Bakwin et al. (1998) and Berger et al. (2001). Three three-axis sonic anemometers at 30, 122, and 396 m above ground are used to measure turbulent winds and virtual potential temperature. Air from these three levels is drawn down tubes to a trailer where three LI-COR 6262 analyzers are used to determine CO_2 and water vapor mixing ratio fluctuations at 5 Hz for eddy covariance flux measurements. The lag times are approximately 16, 23, and 87 s (Berger et al. 2001). High-precision, 2-min mean CO_2 mixing ratios are sampled at six levels (11, 30, 76, 122, 244, and 396 m) by two LI-COR 6251 analyzers (Bakwin et al. 1998). Observations of net radiation, photosynthetically active radiation, and rainfall provide supporting meteorological data.

A National Center for Atmospheric Research (NCAR) Integrated Sounding System (ISS), which includes a radar profiler, a RASS, and a radiosonde system, was deployed about 8 km east of the tower from 15 March to 3 November 1998. The profiler is a sensitive 915-MHz Doppler radar that is designed to respond to fluctuations of the refractive index in clear air (Ecklund et al. 1988; White et al. 1991; Angevine et al. 1993, 1994a,c). The reflectivity measured by the profiler is related to the turbulence intensity, gradients of temperature and humidity, and particulates (Ottersten 1969; VanZandt et al. 1978; Wyngaard et al. 1980; White et al. 1991). The profiler can be used to measure the height of the mixed layer with a time resolution of 30 min or less, a vertical

sampling of 60–100 m, a minimum height of 150 m, and a maximum height of 1500–3000 m depending on conditions (Angevine et al. 1994c). The RASS is an attachment to the profiler that measures temperature profiles up to a height of approximately 800 m above the ground by measuring the vertical propagation of an acoustic pulse (Angevine et al. 1994b). A detailed comparison of wind and temperature measurements from the tower and a similar profiler and RASS is given by Angevine et al. (1998). The ISS also includes a radiosonde system, and sondes were launched about once per week.

The depth of mixed layer can be derived from the signal-to-noise ratio (SNR) recorded by the profiler (Angevine et al. 1994c). The profiler SNR is related to the refractive index structure parameter, C_n^2, in clear air (White et al. 1991). This relationship is based on the assumptions that refractive index irregularities are in equilibrium with steady-state turbulence and that the radar wavelength lies in the inertial subrange of the turbulence (Ottersten 1969). Refractive index varies with both temperature and water vapor fluctuations (Wyngaard and LeMone 1980), however, in the mixed layer C_n^2 is dominated by water vapor. We extract the mixed layer depth, z_i, from the profiler SNR measurements by the method of Angevine et al. (1994c). First, we produce a contour plot of half-hour average range-corrected SNR from the profiler measurements for each day. Second, we define z_i as the median of the heights where SNR peaks occur over the period, as shown in Fig. 1.

Figure 2 shows the profile of potential temperature from a radiosonde launched at 1600 UTC 9 September 1998. UTC is 6 h ahead of local standard time. Here z_i is defined as the location of the sharpest change in potential temperature with height, which occurred at 940 m in this sounding. A 30-min average from the profiler at 1600 UTC gives an estimate for z_i of 850 m, in reasonable agreement with the radiosonde, which represents a point measurement. Turbulent fluctuations in z_i of ± 200 m are common based on lidar observations of the convective PBL (Davis et al. 1997).

The comparison between measurements of z_i made by the radar profiler and from radiosondes launched during the deployment is shown in Fig. 3. The good agreement demonstrates that the z_i can be found accurately from the profiler SNR measurements. However, under unfavorable weather conditions such as precipitation or heavy clouds z_i cannot be estimated from the profiler SNR. Under these conditions the boundary layer is often not clearly defined (Stull 1988). In addition, the profiler is very sensitive to large cloud droplets and raindrops resulting in a high, relatively uniform SNR over the depth of the precipitation shaft.

Mixed layers shallower than 400 m, which typically occur in morning, are not well defined from the profiler SNR measurements. The CO_2 mixing ratio measurements from the tower (e.g., Fig. 4), however, can provide
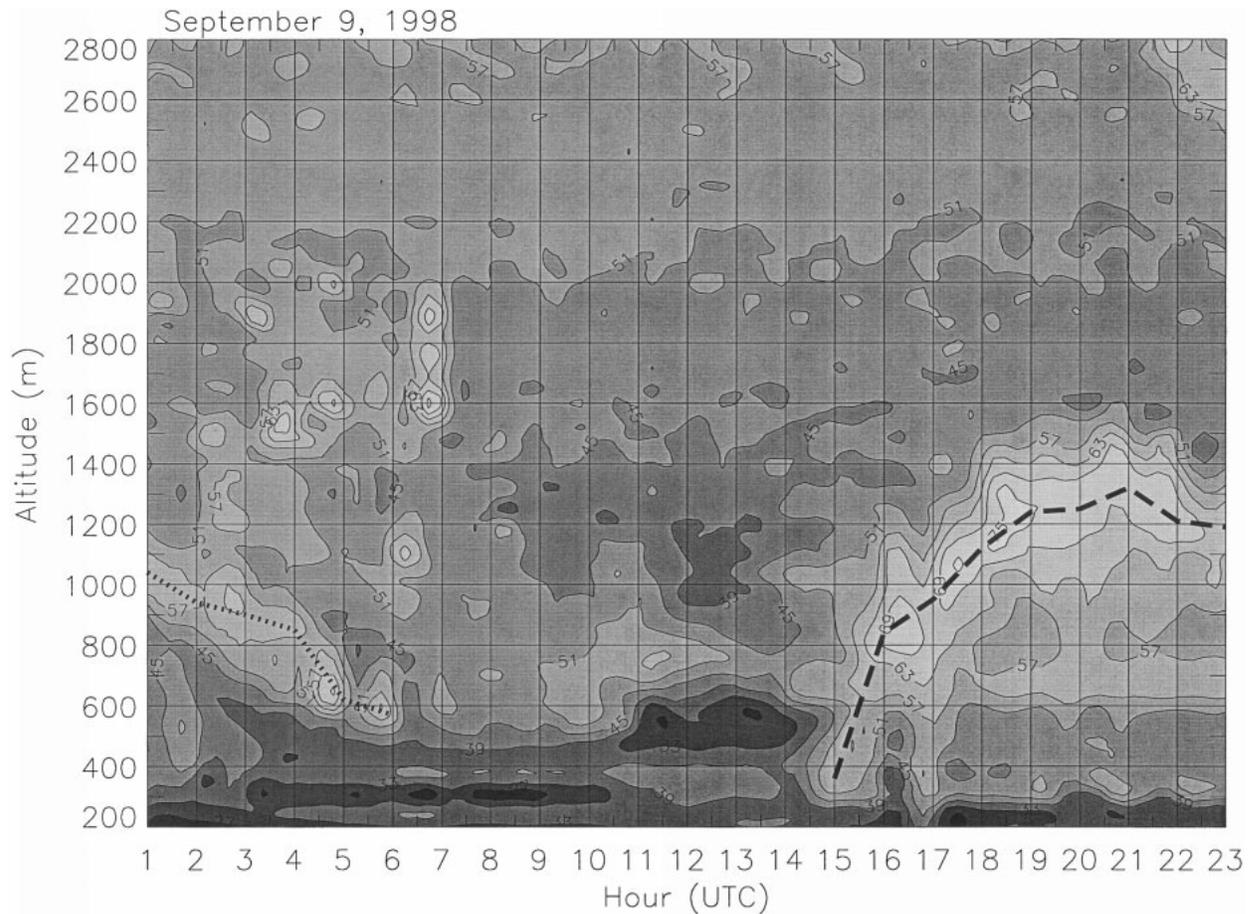
FIG. 1. Development of the mixed layer on 9 Sep 1998 from the radar profiler data. The numbers on the contours are the range-corrected profiler SNR in dB. Long dashed line shows the top of mixed layer and dotted line the top of residual layer. UTC is 6 h ahead of local standard time.

data when z_i is below 400 m. The top of the mixed layer is defined as the depth above ground to which the CO_2 mixing ratio is nearly constant provided that the net radiation is positive (warming the earth's surface).

Stable nocturnal boundary layers are more complicated than the daytime convective PBL. Mahrt et al. (1998) classified stable boundary layers into three different types: a very stable case with a thin, strongly stratified boundary layer; a deep, weakly stratified boundary layer; and an intermediate two-layer stratified boundary layer. It is possible to derive the height for the stable boundary layer from the tower CO_2 mixing ratio measurements because CO_2 is a very good indicator of the stratification. CO_2 released by microbial respiration at night builds up quickly in stable layers close to the ground, and the CO_2 mixing ratio is not altered by radiation like temperature or subject to saturation like water vapor. We define the top of the stable layer as the height at which CO_2 gradients first become very small. For example, as seen in Fig. 4, the heights of the stable layer are estimated to be 20.5, 53, and 183 m (i.e., half-way between adjacent measurement levels)

during the periods of 0000–0300, 0400–1100, and 1200–1300 UTC, respectively. The stable layer, as defined here, typically grows over the course of the night as turbulent mixing from the earth's surface penetrates gradually upward through the stably stratified surface layer. This is consistent with the traditional view of the stable boundary layer (Stull 1988).

Horizontal advection may be important during the morning transition from stable to convective conditions (Yi et al. 2000) and could lead to erroneous identification of the stable layer top. However, for quantification of the depth of the stable layer we neglect cases when the virtual potential temperature flux is positive. As we will show, the CO_2 mixing ratio measurements at the tower allow us to estimate the depth of the stable layer for very stable and moderately stable (intermediate) conditions as defined by Mahrt et al. (1998) and Mahrt (1999), but not for the weakly stable conditions when the stable layer depth often exceeds 400 m. We refer to the very stable and intermediate cases collectively as the stable boundary layer.

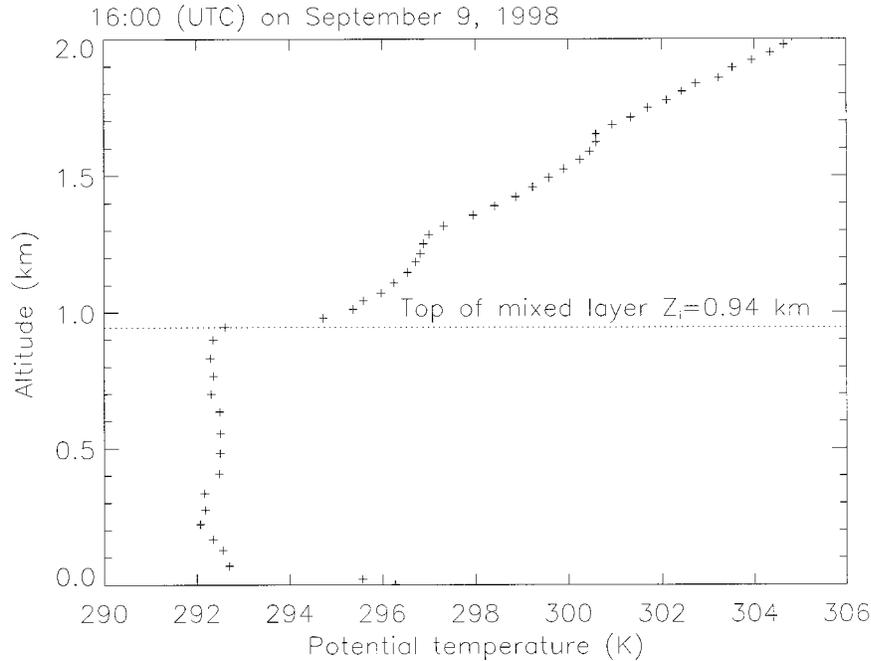Another feature that can be detected by the radar

FIG. 2. The radiosonde profile of potential temperature. The top of the mixed layer (dotted line) is defined as the location of the sharpest change with height in potential temperature.

profiler is the top of the residual mixed layer from the previous day. The top of this residual layer is highlighted by the doted line in Fig. 1. A thin, strongly stratified stable layer also exists near the ground at 0100 UTC, clearly shown by the CO_2 mixing ratio profile (not shown for this day). The top of the residual layer was only observed under very clear and calm nighttime conditions, which typically occurred during periods of synoptic-scale subsidence. These conditions were encountered on three or four nights each month.

3. Results and discussion

a. Convective mixed layer

The monthly averaged diurnal cycles of z_i, net radiation, and sensible and latent heat fluxes are shown in Figs. 5 and 6. The maximum z_i occurs in May, corresponding with maximum sensible heat flux prior to full leaf-out, not maximum net radiation which occurs in July. The surface energy balance in July is maintained by a large latent heat flux due to transpiration. April is also characterized by deep, well-developed mixed layers due to generally large sensible heat fluxes. Here z_i depends on the time-integrated virtual potential temperature flux beginning after sunrise rather than on instantaneous virtual potential temperature flux.

In order to study the relationship between z_i and the cumulative virtual potential temperature flux we use the mixed layer model of Tennekes (1973):

$$\frac{d}{dt}\Delta\Theta = \gamma\left(\frac{dz_i}{dt} - \overline{w}\right) - \frac{\partial\Theta_m}{\partial t}, \qquad (1)$$

$$\frac{\partial\Theta_m}{\partial t} = \frac{1}{z_i}[(\overline{\theta w})_s - (\overline{\theta w})_i], \qquad (2)$$

$$-(\overline{\theta w})_i = \Delta\Theta\left(\frac{dz_i}{dt} - \overline{w}\right), \qquad (3)$$

where Θ_m is mixed layer mean virtual potential temperature, $\Delta\Theta$ is the jump of Θ across the top of the
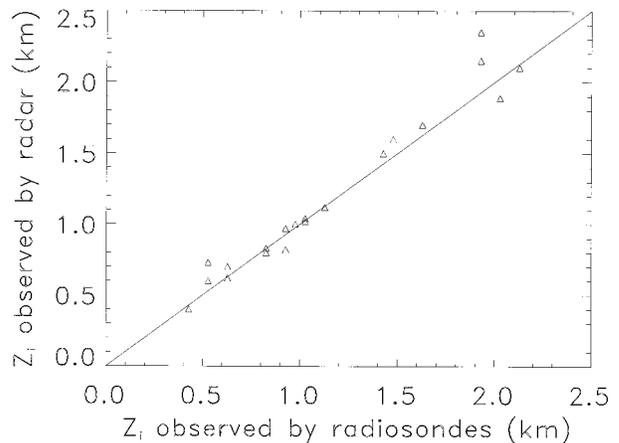

FIG. 3. Comparison of mixed layer depth (z_i) measurements between radar profiler and balloon soundings.
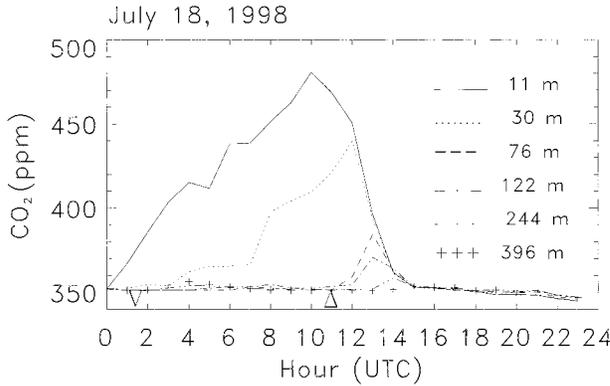
FIG. 4. Profiles of CO_2 mixing ratio for 18 Jul 1998. The depths of the mixed layer can be estimated from the profiles as 20.5, 53, and 320 m, respectively, at 1200, 1300, and 1400 UTC. The heights of the stable layer can be estimated as 20.5, 53, and 183 m during the periods of 0000–0300, 0400–1100, and 1200–1300 UTC, respectively. See text. The triangle indicates sunrise and the inverted triangle indicates sunset.
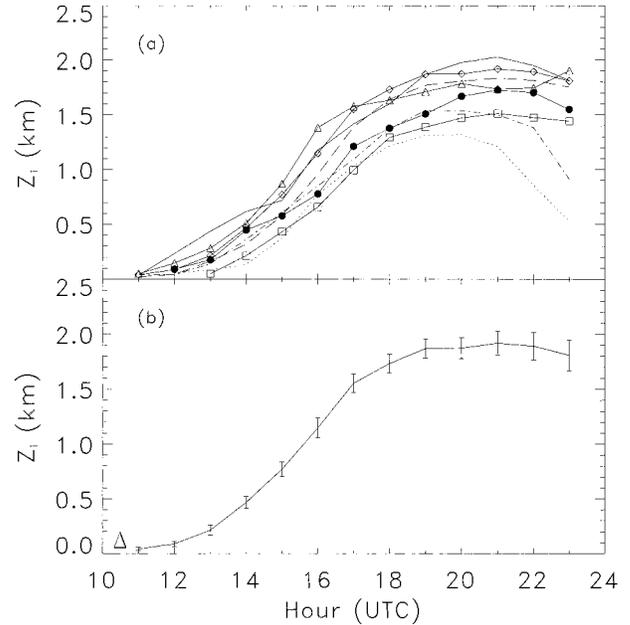

FIG. 5. The diurnal evolution of mixed layer for (a) Mar (square), Apr (filled circle), May (solid line), Jun (triangle), Jul (diamond), Aug (long dashes), Sep (dash–dot line), and Oct (dotted line), and (b) Jul of 1998. They have similar standard deviation of mean (error bars) as shown in (b). The triangle in (b) indicates sunrise for July. The mixed layer depths were derived from radar profiler and CO_2 mixing ratio measurements.

mixed layer, $(\overline{\theta w})$ is virtual potential temperature flux, subscript s and i refer to the surface and z_i, respectively, γ denotes the lapse rate ($= \partial\Theta/\partial z$) above the top of the mixed layer, and $\overline{w}$ is the mean vertical velocity at z_i. The entrainment velocity is given by

$$w_e = dz_i/dt - \overline{w}. \qquad (4)$$

Heating of the PBL air acts to decrease $\Delta\Theta$, while $\Delta\Theta$ increases at the rate γw_e associated with entrainment. The subsidence effect was neglected in Tennekes' model because $\overline{w}$ is usually smaller than dz_i/dt and is difficult to observe directly. However, the terms associated with $\overline{w}$ are included here to give an understanding of how the subsiding motion affects mixed layer growth. The influence of shear on z_i is neglected. Mahrt and Lenschow (1976) found that shear contributions are important only for small z_i or weak stratification above z_i. Additional discussion regarding entrainment can be found in Tennekes (1973), Tennekes and Driedonks (1981), and Deardorff (1979).

If γ is taken to be constant, the solution of (1)–(3) is

$$\Delta\Theta z_i - (\Delta\Theta z_i)_0$$

$$= \frac{1}{2}\gamma(z_i^2 - Z_{i0}^2) - \int_0^t [(\overline{\theta w})_s + \overline{w}(\gamma z_i - \Delta\Theta)]\, dt',$$

$$(5)$$

where the subscript 0 refers to values at the time when $(\overline{\theta w})_s$ changes sign from negative to positive. In order to determine z_i from (5) we reduce the unknowns by employing a simple relationship between the entrainment flux and the surface flux,

$$-(\overline{\theta w})_i = c(\overline{\theta w})_s, \qquad (6)$$

where c is an empirically determined constant. This linear relation is based on analysis of the turbulent kinetic energy budget. Although Zilitinkevich (1975) gave a more precise expression for c, we assume it to be constant here. Most of the published values of c lie between 0.1 and 0.3 (Stull 1976; Barr and Betts 1997; Davis et al. 1997) though some observations suggest values as large as 0.4–0.5 (Betts et al. 1992; Angevine et al. 1998). Combining (6) with (1)–(3) and assuming $\overline{w} = 0$ yields

$$\Delta\Theta z_i^{1+c^{-1}} = (\Delta\Theta)_0 Z_{i0}^{1+c^{-1}}$$

$$+ \frac{\gamma}{2 + c^{-1}}(z_i^{2+c^{-1}} - Z_{i0}^{2+c^{-1}}). \qquad (7)$$

Neglecting the terms in (7) related to Z_{i0} is an excellent approximation because of the large powers of z_i. Thus, the relationship of $\Delta\Theta$ to z_i becomes

$$\Delta\Theta = \frac{\gamma z_i}{2 + c^{-1}}. \qquad (8)$$

It is also a good approximation to neglect the initial term on the right-hand side of (5) when $z_i > 3Z_{i0}$. Hence, substitution of (8) into (5) gives

$$z_i \approx \left[\frac{2(2c + 1)}{\gamma}\int_0^t (\overline{\theta w})_s\, dt' + 2(1 + c)\int_0^t \overline{w}z_i\, dt'\right]^{1/2}.$$

$$(9)$$

Hence, z_i is proportional to the square root of the cumulative $(\overline{\theta w})_s$. However, we note that (9) is only valid during the period when the mixed layer is growing, (3) breaks down as w_e becomes zero (i.e., $dz_i/dt = \overline{w}$). If
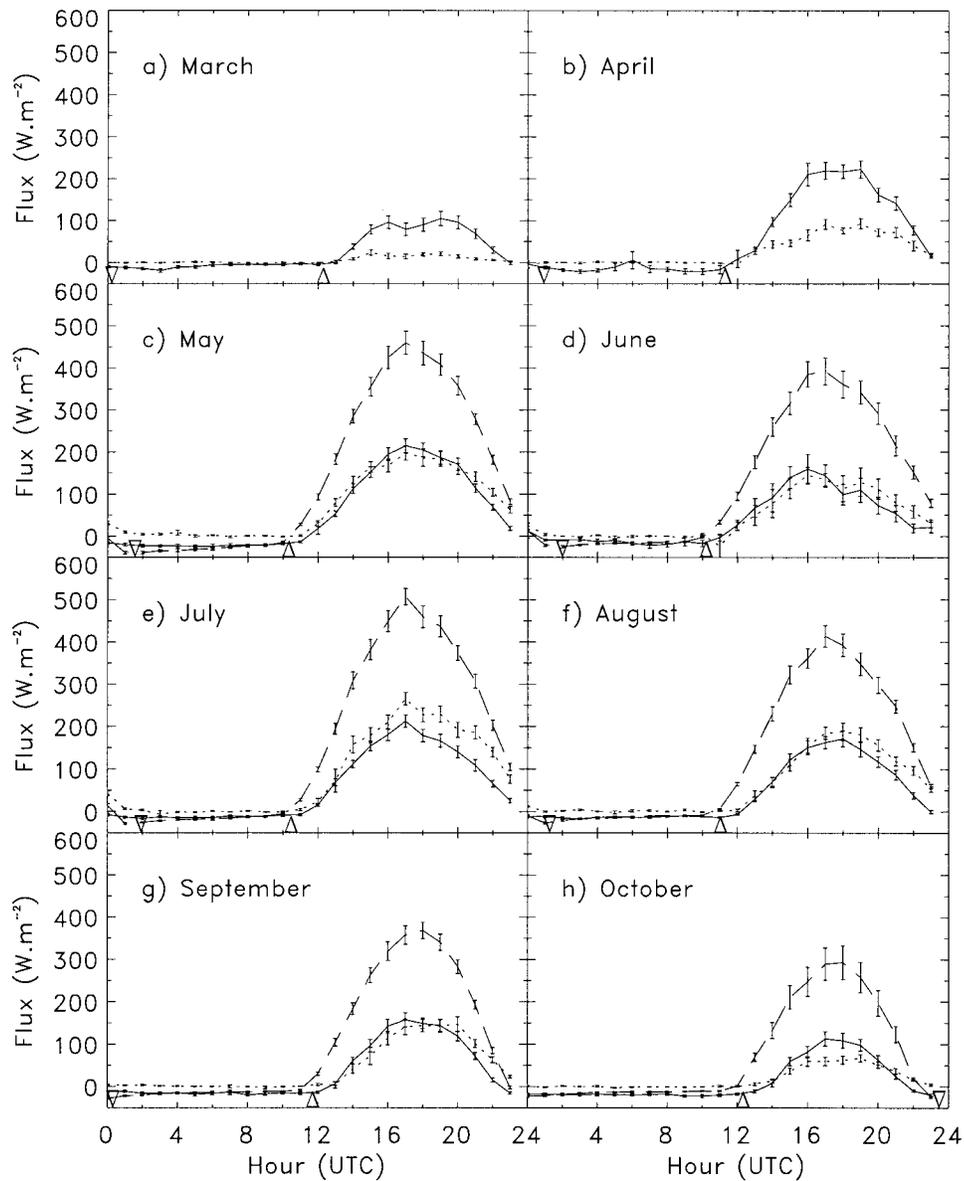
FIG. 6. The diurnal evolution of net radiation (dashed line), sensible heat flux (solid line), and latent heat flux (dotted line). The triangles indicate sunrise and the inverted triangles indicate sunset. Net radiation data are missing for Mar and Apr due to an instrumental problem. The sensible heat and latent heat fluxes were measured at 30 m and net radiation at 2 m.

subsidence is negligible (3) is valid only until the mixed layer reaches its maximum depth, otherwise, it is valid until the mixed layer reaches maximum depth and dz_i/dt becomes equal to $\overline{w}$.

The last term in (9) is negative when $\overline{w} < 0$ (subsidence). While $\overline{w}$ should be positive when the study site is in a low-pressure region, the top of the mixed layer is often difficult to define in this situation. Therefore, we focus here on a discussion of subsidence. In order to estimate the magnitude of the change in z_i caused by subsidence we assume $\overline{w}$ to be constant, which is reasonable over the course of a day since sub-

sidence is a synoptic-scale phenomenon, and we drop the first term in (9) to obtain

$$(\Delta z_i)_{\text{subsidence}} \approx (1 + c)\overline{w}t. \qquad (10)$$

If we take $\overline{w} = -0.01$ to -0.03 m s^{-1}, $c = 0.2$ and $t = 8$ h, then subsidence will cause the mixed layer depth to shrink by 350–1040 m. Therefore, a 20%–60% reduction of z_i could be caused by subsidence.

Figure 7 shows the relationship between z_i and

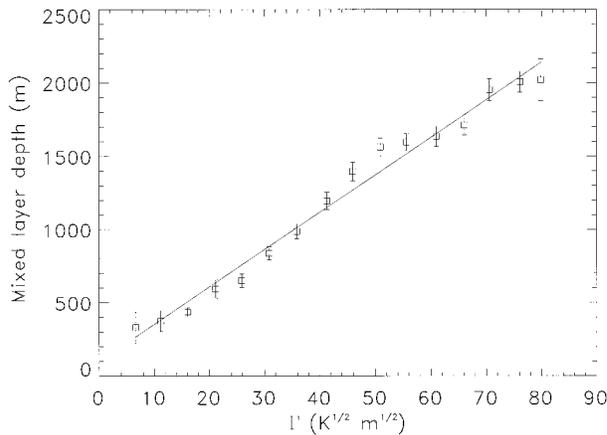$$\Gamma = \sqrt{\int_0^t (\overline{\theta w})_s \, dt'},$$

FIG. 7. The relationship of mixed layer depth (z_i) with the square root of the cumulative surface virtual potential temperature flux,

$$\Gamma = \sqrt{\int_0^t (\overline{\theta w})_s \, dt'}.$$

Each point is the average value of z_i over each 5 $K^{1/2}$ $m^{1/2}$ of Γ. The error bars show ± 1 standard deviation of mean. All data are for the period of the mixed layer growth. The solid line is a linear fit to the data.

along with a least squares linear fit to the data ($r^2 = 0.98$). Only data within the period when the mixed layer was growing were used. The linear fit is given by

$$z_i = a + b\Gamma, \quad (11)$$

where $a = 97.1$ m and $b = 25.537$ $K^{-1/2}$ $m^{1/2}$. This linear relationship between z_i and Γ is in good agreement with the theoretical prediction (9). The only approximations in (9) we have made are that γ and c are constants and the initial terms in (5) have been neglected. As seen from Fig. 5, 2 h is typically sufficient for the mixed layer to grow up more than $3Z_{i0}$. A weak nonlinear relationship between z_i and Γ in Fig. 7 could result from a change in γ. The lapse rate can be estimated as $\gamma \approx 2(2c + 1)/b^2$ in (K m^{-1}) by combining the linear term in (11) with (9) and by neglecting the subsidence term. If $c = 0.2$, then $\gamma \approx 4.3$ K km^{-1}.

A more rigorous derivation of (10) suggested by Lanschow (2000, personal communication) can be found in the appendix. This derivation assumes constant flux divergence rather than constant $\overline{w}$, which is a more reasonable assumption, especially when z_i is small.

A remaining question is: How can we determine, from the measurements of $(\overline{\theta w})_s$, when the mixed layer reaches its maximum depth? In general, the mixed layer does not stop growing as $(\overline{\theta w})_s$ reaches its maximum value, but continues for some time depending on weather conditions and season. The frequency distribution of this time lag is shown in Fig. 8. Because of data selection, the weather conditions vary somewhat for the data in Fig. 8. Three hours is the dominant lag, and this case includes cloudy days in summertime and clear days in the months of March, April, and October. The weather conditions for 2-h lags are similar to 3-h lags. However,
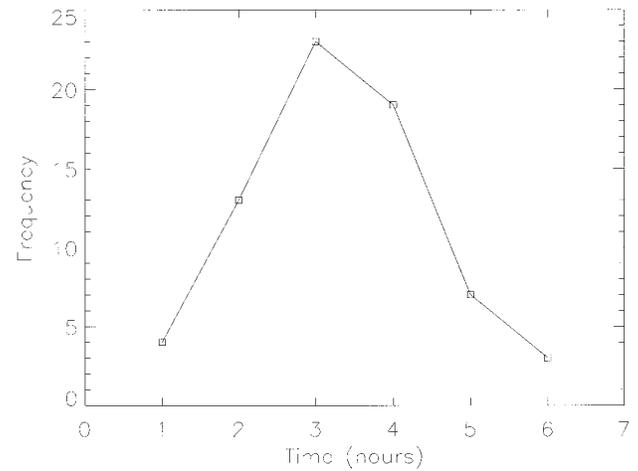

FIG. 8. Frequency distribution of the number of hours after the time of maximum surface virtual potential temperature flux, $(\overline{\theta w})_s$, to the time of the maximum depth of the mixed layer, z_i.

the weather is generally clear or partly cloudy on days when maximum z_i is reached 4 h after maximum $(\overline{\theta w})_s$. With clear skies in the summertime, the mixed layer can continue to grow for 5 or 6 h after the maximum $(\overline{\theta w})_s$ since energy input is still substantial even with low sun angles. However, energy input often limits mixed layer growth during the spring and fall months, and during cloudy days in summer. We conclude that, to a reasonable approximation, z_i may be calculated integrating (11) to 2 h after $(\overline{\theta w})_s$ reaches its maximum, after which the rate of growth slows significantly.

b. Stable layer

On calm nights, respiration results in the accumulation of CO_2 near the ground. The respiration rate depends mainly on temperature of the surface soil, which changes slowly with time, hence CO_2 is a good indicator for the strength of stratification of a stable boundary layer. As seen in Fig. 4, the difference in CO_2 mixing ratio between 11 and 76 m reached nearly 130 ppm at 1000 UTC 18 July 1998. The difference in CO_2 mixing ratio between 11 and 30 m can sometimes reach 140 ppm under very stable conditions on calm nights. On windy nights, CO_2 mixing ratios at all measurement levels are nearly uniform. For the weakly stratified situation, CO_2 mixing ratios at all levels behave alike and the height of the stable layer is above 400 m. Therefore, we focus on the stable case as previously defined. The diurnal variation of the stable layer depth from March through October of 1998 is shown in Fig. 9. The common feature is that the stable layer height increases with time during night. In summertime, the stable layer heights are very low in early evening, typically below 30 m.

The CO_2 data show that, under very stable conditions, intermittent turbulence occurs near the surface and is damped out very quickly with height. The strength of this shear-generated turbulence can be indicated by the
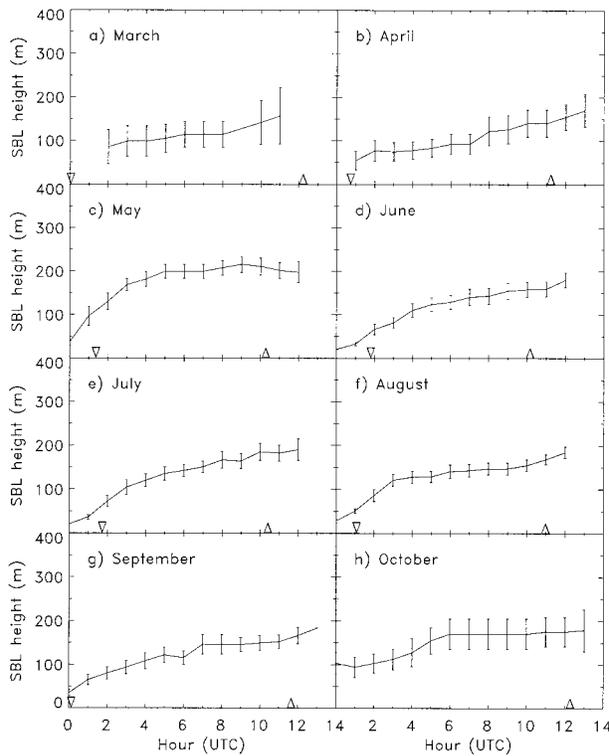
FIG. 9. The diurnal evolution of stable layer from Mar through Oct 1998. The stable layer height was derived from CO_2 mixing ratio measurements. The triangles indicate sunrise and the inverted triangles indicate sunset.

FIG. 10. Relationship between friction velocity, u_*, and surface sensible heat flux, H, at night. The dashed line ($L = 100$) divides the space into a weakly stable ($L > 100$) and a stable ($L < 100$) region. Data corresponding to Fig. 9 are given by filled circles, and other data are shown as triangles.

friction velocity, u_*. On the other hand, the development of the stable layer is closely related to sensible heat flux H. Mahrt et al. (1998) describe three regions in the space defined by u_* and H based on the stability, z/L, where L is the Obukhov length: the weakly stable case; the transition case; and the very stable case. Figure 10 shows hourly data for H and u_* observed at 30 m at night. Points corresponding to the data used in Fig. 9 are shown by filled circles in Fig. 10. They are concentrated in the very stable and transition region, which is similar to Fig. 3 in Mahrt et al. (1998). The nearly linear relationship between u_* and H is expected because both the friction velocity and the sensible heat flux are related to the intensity of the turbulence. It appears that the deepest stable layers are associated with high u_* and, to a lesser extent, strongly negative H values.

c. Residual layer and mean vertical velocity

Figure 11 shows the mean diurnal pattern of the residual, stable, and mixed layer depths. These diurnal averages were made only with data obtained on dates when the residual layer could be identified from the profiler SNR (Table 1). Surface synoptic weather maps show that these conditions were characterized by high barometric pressure and clear skies, with the site typi-
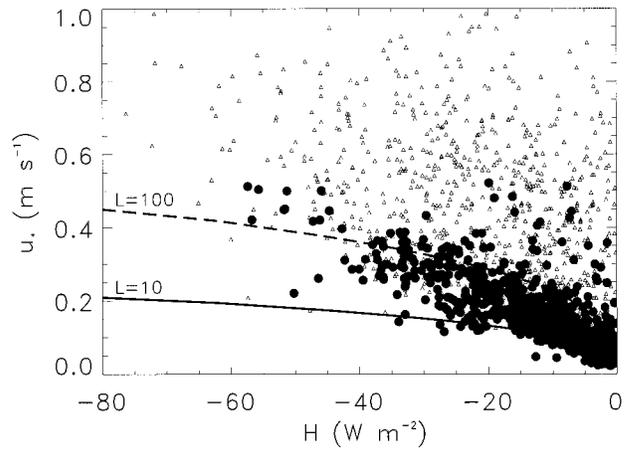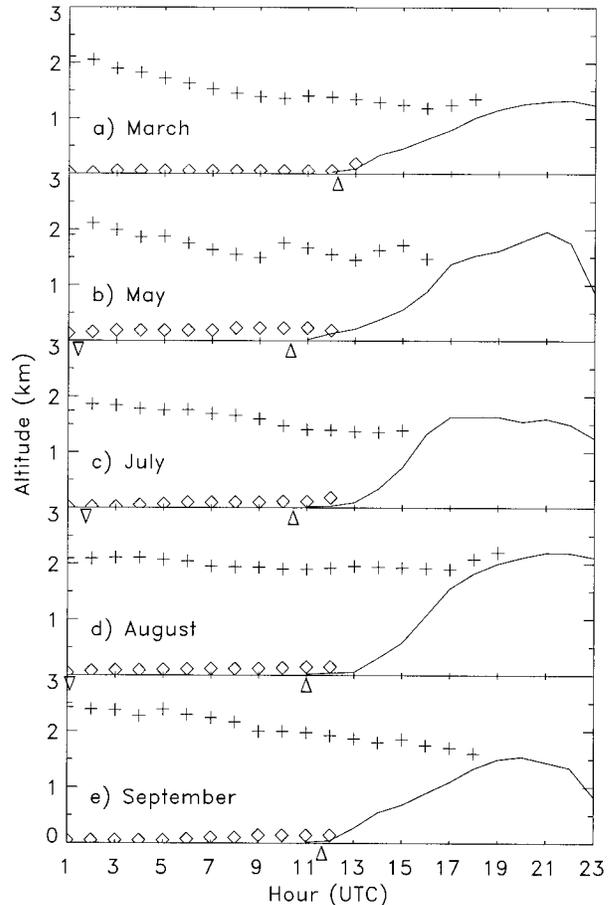

FIG. 11. Diurnal evolution of residual layer (plus), mixed layer (solid line), and stable layer (diamond) for cases of calm, clear nights with subsidence. The triangles indicate sunrise and the inverted triangles indicate sunset. The dates are the same as in Table 1.

TABLE 1. Estimate of mean vertical velocity based on the profiler SNR data.

Date (1998)	Mean vertical velocity (m s^{-1})
17 Mar	-0.013
20 Mar	-0.019
24 Mar	-0.027
3 Apr	-0.029
23 Apr	-0.015
14 May	-0.067
20 May	-0.030
25 May	-0.030
17 Jul	-0.037
18 Jul	-0.002
26 Jul	-0.018
1 Aug	-0.011
2 Aug	-0.005
11 Aug	-0.010
15 Aug	-0.001
31 Aug	-0.003
4 Sep	-0.018
10 Sep	-0.038
23 Sep	-0.008

cally located at or near a high-pressure center. On those days horizontal winds must be light, otherwise the residual layer structure would be disrupted due to shear effects. Hence, it is likely that the observed reduction in the depth of the residual layer during the night for all months (Fig. 11) is caused by subsidence, and we can calculate the mean synoptic vertical velocity ($\overline{w}$, subsidence rate) using (10) with $c = 0$. The results (Table 1) are in reasonable accord with estimates obtained by scaling analysis. The mean vertical velocities in August were smaller than the other months.

The evolution of the residual, stable, and mixed layers as shown in Fig. 11 occurred on and after clear, calm nights with subsidence. The sequence of events on these days is as follows. Around sunset the upward $(\overline{\theta w})_s$ becomes zero or negative (downward) due to radiative cooling. Consequently, a stable layer is formed near the surface and the mixed layer becomes a neutrally stratified residual layer. The residual layer is almost isolated from the ground by the stable layer. The stable layer air, with very high CO_2 mixing ratio, becomes entrained into the mixed layer shortly after sunrise and subsequently the mixed layer grows through the residual layer, which is characterized by relatively uniform CO_2 with height. The mixed layer depth usually reaches the top of the residual layer at about noon local time (1800 UTC).

Comparing cases with clearly defined subsidence (Fig. 11) with all cases (Fig. 5) we observe that z_i is reduced in the former except in August and September. However, the subsidence in August was apparently very weak, and coupled with strong $(\overline{\theta w})_s$, may explain why z_i in Fig. 11d is deeper than the one in Fig. 5.

d. CO$_2$ jump

The tower data (Fig. 4) can be used to determine the nocturnal pattern of the CO_2 jump across the inversion, which we define as the difference in CO_2 mixing ratio between 11 and 396 m. Above the 200-m level CO_2 mixing ratios are usually constant with time under stable conditions at night. Therefore, the CO_2 mixing ratio at 396 m can be considered typical of the residual layer. With disturbed weather conditions such as precipitation, heavy clouds, or wind the CO_2 mixing ratios at all six levels are similar and the CO_2 jump is very small. The data when the stable layer is deeper than 400 m are excluded in Fig. 12. After formation of a stable layer begins, the CO_2 jump increases until sunrise when convective mixing begins. The decrease in the CO_2 jump in the morning shown in Fig. 12 is caused by photosynthesis, turbulent mixing, and possibly by advection (Yi et al. 2000). Measurements of the biogenic tracer CH_4 indicate that photosynthesis begins somewhat earlier in the morning than does convective growth of the mixed layer (D. Hurst and P. Bakwin 1998, unpublished data). The seasonal change in the nocturnal pattern of the CO_2 jump is considerable due mainly to seasonal changes in respiration.

4. Concluding remarks

The depth of the mixed layer, z_i, has been derived by the combination of 915-MHz radar SNR and CO_2 mix-
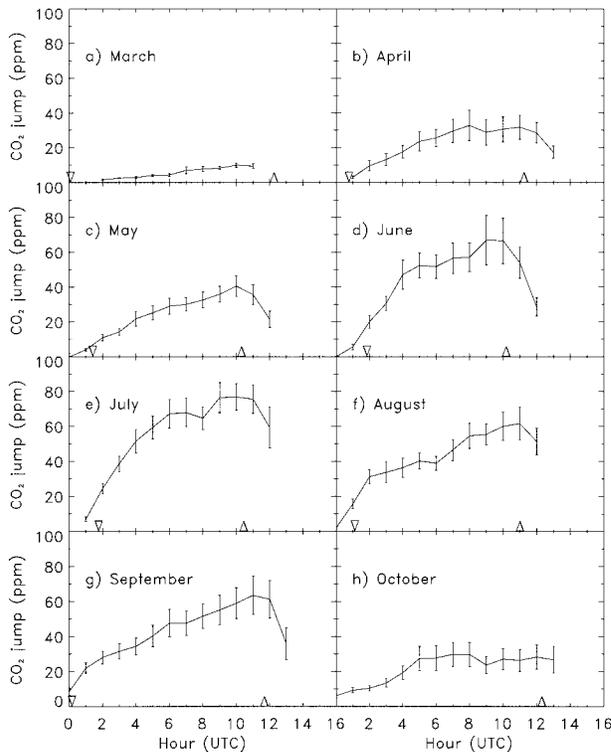

FIG. 12. Nocturnal evolution of the difference in CO_2 mixing ratio between 11 and 396 m from Mar through Oct 1998. The data when the stable layer is deeper than 400 m are excluded. The triangles indicate sunrise and the inverted triangles indicate sunset.

ing ratio measurements from a very tall tower. An empirical relationship between z_i and the square root of the cumulative surface virtual potential temperature flux,

$$\Gamma = \sqrt{\int_0^t (\overline{\theta w})_s \, dt'},$$

is obtained ($r^2 = 0.98$) for this site. Insofar as the mixed layer model is valid, this result should apply to other locations. This model can be used to predict mean z_i during the period of the day when the mixed layer grows due to surface heating. There may be need for minor adjustment to the coefficients in (11) if the measuring height for $(\overline{\theta w})_s$ is not at 30 m, as was used in this study.

The heights of nocturnal stable boundary layers were derived based on CO_2 mixing ratio measurements from the tall tower. The stable boundary layer heights typically increased over the course of the night. The weakly stable cases and windy nights were excluded because the height of boundary layer is greater than the tower height for those cases.

Subsidence has different influences on the evolution of the mixed, stable, and residual layers. Nighttime conditions when subsidence occurs generally have clear skies and strong radiative cooling that favor the development of a stable layer, trapping cold air near the ground. The divergence associated with subsidence suppresses growth of the stable layer somewhat. During the daytime, z_i depends on the competition between growth due to virtual potential temperature flux and reduction due to subsidence. The larger $(\overline{\theta w})_s$ caused by the clear skies under conditions of subsidence favor increased growth of the mixed layer, but subsidence itself reduces z_i, as can be estimated by (10). We observed that a 10%–20% reduction in z_i could be caused by subsidence, based on comparison of Figs. 11 and 5, and excluding August and September. For August, a nearly 15% increase in z_i resulted from the fact that clear skies and drier air favored greater $(\overline{\theta w})_s$, and $\overline{w}$ was small (Table 1).

The residual layer was observed only on nights when the study site was under a synoptic high pressure system. We estimated the subsidence rate ($\overline{w}$) as equal to the rate at which the residual layer top moved downward during the night (Table 1). Equation (10) should be valid for the residual layer as a result of (9) with $(\overline{\theta w})_s = 0$. We estimated the mean vertical velocities using (10), with $c = 0$.

APPENDIX

Discussion of Limiting Cases of (9)

In order to discuss the limiting cases, (9) can be written as a differentiate form

$$z_i \frac{dz_i}{dt} = \frac{(2c + 1)}{\gamma}(\overline{\theta w})_s + (1 + c)\overline{w}z_i. \quad (A1)$$

We assume $(\overline{\theta w})_s$ and $\overline{w}$ to be constant, then (A1) becomes

$$z_i \frac{dz_i}{dt} + Az_i = B, \quad (A2)$$

where

$$A = -(1 + c)\overline{w}, \quad (A3)$$

$$B = \frac{2c + 1}{\gamma}(\overline{\theta w})_s. \quad (A4)$$

By integrating (A2), we obtain

$$t = -\frac{z_i - z_{i0}}{A} + \frac{B}{A^2} \ln\left(\frac{Az_{i0} - B}{Az_i - B}\right). \quad (A5)$$

Here z_{i0} is the mixed layer depth at $t = 0$.

We now consider the limiting case of small A, that is, $B \gg z_{i0}A$ or $(\overline{\theta w})_s \gg -[(1 + c)\gamma]/(2c + 1)\overline{w}z_{i0}$. Since

$$\ln(1 - x) = -x - \frac{x^2}{2} - \frac{x^3}{3} - \cdots, \quad (|x| < 1) \quad (A6)$$

(A5) can be expanded into the Taylor's series

$$t = -\frac{z_i - z_{i0}}{A} + \frac{B}{A^2} \ln\left(\frac{1 - \dfrac{Az_{i0}}{B}}{1 - \dfrac{Az_i}{B}}\right)$$

$$= \frac{1}{2B}(z_i^2 - z_{i0}^2) + \frac{A}{3B^2}(z_i^3 - z_{i0}^3) + \cdots. \quad (A7)$$

Thus

$$z_i \cong \sqrt{2Bt + H^2} = \sqrt{\frac{2(2c + 1)}{\gamma}(\overline{\theta w})_s t + z_{i0}^2}. \quad (A8)$$

Therefore, for small $2Bt$, one would expect that the measured z_i will be larger than z_i estimated by the relation $z_i \sim 2Bt$ since z_{i0} is neglected in (9).

Similarly, for another limiting case $B \ll Az_{i0}$ or $(\overline{\theta w})_s \ll -\{[(1 + c)]\gamma\}/(1 + 2c)\}\overline{w}z_{i0}$, we can obtain

$$t \cong -\frac{z_i - z_{i0}}{A} + \frac{B}{A^2} \ln\frac{z_{i0}}{z_i}. \quad (A9)$$

Therefore, we can say that

$$z_i - z_{i0} \cong -At = (1 + c)\overline{w}t, \quad (A10)$$

with the condition $B \ll A^2 t/|\ln(z_{i0}/z_i)|$, that is, $(\overline{\theta w})_s \ll [(1 + c)^2\gamma\overline{w}^2 t]/[(1 + 2c)|\ln(z_{i0}/z_i)|]$.

We now use an alternative assumption for the mean vertical velocity, $\overline{w} = Dz$. This constant divergence assumption is probably more realistic, especially for small z_i. Then, (A1) becomes

$$z_i \frac{dz_i}{dt} + A'z_i^2 = B, \quad (A11)$$

where

$$A' = -(1 + c)D. \tag{A12}$$

It is easy to obtain the solution of (A11)

$$t = \frac{1}{2A'} \ln\left(\frac{B - A'z_{i0}^2}{B - A'z_i^2}\right). \tag{A13}$$

For $A'z_{i0}^2 \ll B$,

$$t = \frac{1}{2A'}\left[\frac{A'}{B}(z_i^2 - z_{i0}^2) + \frac{1}{2}\frac{A'^2}{B^2}(z_i^4 - z_{i0}^4) + \cdots\right]$$

$$\cong \frac{1}{2B}(z_i^2 - z_{i0}^2). \tag{A14}$$

Therefore,

$$z_i \cong \sqrt{2Bt + z_{i0}^2}, \tag{A15}$$

which is the same relation as (A8) due to subsidence term is neglected in both cases.

For $B \ll A'z_{i0}^2$, from (A13) we obtain

$$t \cong \frac{1}{2A'} \ln\frac{z_{i0}^2}{z_i^2}. \tag{A16}$$

Thus

$$z_i = z_{i0} \exp(-A't). \tag{A17}$$

For small t, by expanding (A17) into Taylor's series, we get

$$z_i - z_{i0} = -A'z_{i0}t = (1+c)Dz_{i0}t = (1+c)\overline{w}_0t. \tag{A18}$$

Here $\overline{w}_0$ is the mean vertical velocity at $t = 0$. (A10) and (A18) are very similar, however, the assumption of constant divergence is more reasonable than constant $\overline{w}$ when z_i is small.

REFERENCES

Angevine, W. M., S. K. Avery, W. L. Ecklund, and D. A. Carter, 1993: Fluxes of heat and momentum measured with a boundary-layer wind profiler radar-radio acoustic sounding system. *J. Appl. Meteor., 32,* 73–80.
——, R. J. Doviak, and Z. Sorbjan, 1994a: Remote sensing of vertical velocity variance and surface heat flux in a convective boundary layer. *J. Appl. Meteor., 33,* 977–983.
——, W. L. Ecklund, D. A. Carter, K. S. Gage, and K. P. Moran, 1994b: Improved radio-acoustic sounding techniques. *J. Atmos. Oceanic Technol., 11,* 42–49.
——, A. B. White, and S. K. Avery, 1994c: Boundary-layer depth and entrainment zone characterization with a boundary-layer profiler. *Bound.-Layer Meteor., 68,* 375–385.
——, P. S. Bakwin, and K. J. Davis, 1998: Wind profiler and RASS measurements compared with measurements from a 450-m tall tower. *J. Atmos. Oceanic Technol., 15,* 818–825.
Bakwin, P. S., P. P. Tans, D. F. Hurst, and C. Zhao, 1998: Measurements of carbon dioxide on very tall towers: Results of the NOAA/CMDL program. *Tellus, 50B,* 401–415.
Barr, A. G., and A. K. Betts, 1997: Radiosonde boundary layer budgets above a boreal forest. *J. Geophys. Res., 102,* 29 205–29 212.
Berger, B. W., K. J. Davis, C. Yi, P. S. Bakwin, and C. Zhao, 2001: Long-term carbon dioxide fluxes from a very tall tower in a northern forest: Flux measurement methodology. *J. Atmos. Oceanic Technol., 18,* 529–542.
Betts, A. K., R. L. Desjardins, and J. I. MacPherson, 1992: Budget analysis of the boundary layer grid flights during FIFE 1987. *J. Geophys. Res., 97,* 18 533–18 546.
Ciais, P., P. P. Tans, M. Trolier, J. White, and R. Francey, 1995: A large Northern Hemisphere terrestrial sink indicated by the ^{13}C/^{12}C ratio of atmospheric CO_2. *Science, 269,* 1098–1102.
Davis, K. J., D. H. Lenschow, S. P. Oncley, C. Kiemle, G. Ehret, A. Giez, and J. Mann, 1997: Role of entrainment in surface–atmosphere interactions over the boreal forest. *J. Geophys. Res., 102,* 29 219–29 230.
Deardorff, J. W., 1979: Prediction of convective mixed-layer entrainment for realistic capping inversion structure. *J. Atmos. Sci., 36,* 424–436.
Denning, A. S., I. Y. Fung, and D. Randall, 1995: Latitudinal gradient of atmospheric CO_2 due to seasonal exchange with land biota. *Nature, 376,* 240–243.
——, D. A. Randall, G. J. Collatz, and P. J. Sellers, 1996: Simulations of terrestrial carbon metabolism and atmospheric CO_2 in a general circulation model. Part 2: Simulated CO_2 concentrations. *Tellus, 48B,* 543–567.
——, T. Takahashi, and P. Friedlingstein, 1999: Can a strong atmospheric CO_2 rectifier effect be reconciled with a ''reasonable'' carbon budget? *Tellus, 51B,* 249–253.
Ecklund, W. L., D. A. Carter, and B. B. Balsley, 1988: A UHF wind profiler for the boundary layer: Brief description and initial results. *J. Atmos. Oceanic Technol., 5,* 432–441.
Fan, S., M. Gloor, J. Mahlman, S. Pacala, J. Sarmiento, T. Takahashi, and P. Tans, 1998: A Large terrestrial carbon sink in North America implied by atmospheric and oceanic carbon dioxide data and models. *Science, 282,* 442–446.
Francey, R. J., P. O. Tans, C. E. Allison, I. G. Enting, J. W. C. White,

and M. Trolier, 1995: Changes in oceanic and terrestrial carbon uptake since 1982. *Nature,* **373,** 326–330.

Law, R. M., and P. J. Raymer, 1999: Impacts of seasonal covariance on CO2 inversions. *Global Biogeochem. Cycles,* **13,** 845–856.

Mahrt, L., 1999: Stratified atmospheric boundary layers. *Bound.-Layer Meteor.,* **90,** 375–396.

——, and D. H. Lenschow, 1976: Growth dynamics of the convectively mixed layer. *J. Atmos. Sci.,* **33,** 41–51.

——, J. Sun, W. Blumen, T. Delany, and S. Oncley, 1998: Nocturnal boundary-layer regimes. *Bound.-Layer Meteor.,* **88,** 255–278.

Ottersten, H., 1969: Atmospheric structure and radar backscattering in clear air. *Radio Sci.,* **4,** 1179–1193.

Stull, R. B., 1976: The energetics of entrainment across a density interface. *J. Atmos. Sci.,* **33,** 1260–1267.

——, 1988: *An Introduction to Boundary-Layer Meteorology.* Kluwer, 666 pp.

Tans, P. P., I. Y. Fung, and T. Takahashi, 1990: Observational constraints on the global atmospheric CO_2 budget. *Science,* **247,** 1431–1438.

Tennekes, H., 1973: A model for the dynamics of the inversion above a convective boundary layer. *J. Atmos. Sci.,* **30,** 558–567.

——, and A. G. M. Driedonks, 1981: Basic entrainment equations for the atmospheric boundary layer. *Bound.-Layer Meteor.,* **20,** 515–531.

VanZandt, T. E., J. L. Green, K. S. Gage, and W. L. Clark, 1978: Vertical profiles of refractivity turbulence structure constant: Comparison of observation by the sunset radar with a new theoretical model. *Radio Sci.,* **13,** 819–829.

White, A. B., C. W. Fairall, and D. W. Thompson, 1991: Radar observations of humidity variability in and above the marine atmospheric boundary layer. *J. Atmos. Oceanic Technol.,* **8,** 639–658.

Wofsy, S. C., R. C. Harriss, and W. A. Kaplan, 1988: Carbon dioxide in the atmosphere over the Amazon basin. *J. Geophys. Res.,* **93,** 1377–1387.

Wyngaard, J. C., and M. A. LeMone, 1980: Behavior of the refractive index structure parameter in the entraining convective boundary layer. *J. Atmos. Sci.,* **37,** 1573–1585.

Yi, C., K. J. Davis, P. B. Bakwin, B. W. Berger, and L. C. Marr, 2000: The influence of advection on measurements of the net ecosystem–atmosphere exchange of CO_2 from a very tall tower. *J. Geophys. Res.,* **105,** 9991–9999.

Zilitinkevich, S. S., 1975: Comments on "A model for the dynamics of the inversion above a convective boundary layer." *J. Atmos. Sci.,* **32,** 991–992.